optica

Infrared nanospectroscopic imaging in the rotating frame

Samuel C. Johnson,[1] Eric A. Muller,[1] Omar Khatib,[1] Elisa A. Bonnin,[2] Alexander C. Gagnon,[2] and Markus B. Raschke[1,*]

[1]*Department of Physics, Department of Chemistry, and JILA, University of Colorado, Boulder, Colorado 80309, USA*
[2]*School of Oceanography, University of Washington, Seattle, Washington 98195, USA*
Corresponding author: markus.raschke@colorado.edu

Infrared (IR) vibrational scattering scanning near-field optical microscopy (*s*-SNOM) has advanced to become a powerful nanoimaging and spectroscopy technique with applications ranging from biological to quantum materials. However, full spatiospectral *s*-SNOM continues to be challenged by long measurement times and drift during the acquisition of large associated datasets. Here, we demonstrate a novel approach of computational spatiospectral *s*-SNOM by transforming the basis from the stationary frame into the rotating frame of the IR carrier frequency. We demonstrate an acceleration of IR *s*-SNOM data collection by a factor of 10 or more in combination with prior knowledge of the electronic or vibrational resonances to be probed, the IR source excitation spectrum, and other general sample characteristics. As an example, we apply rotating-frame *s*-SNOM (R-sSNOM) to chemical nanoimaging of ultrathin protein sheets in a mollusk shell. R-sSNOM enables high-voxel-density imaging of sparsely distributed molecules in an extended matrix. It is generally applicable to many multiscale material systems with sparse features and can be extended to other spectroscopic nanoimaging modalities.   © 2019 Optical Society of America under the terms of the OSA Open Access Publishing Agreement

https://doi.org/10.1364/OPTICA.6.000424

1. INTRODUCTION

Recent advances in infrared (IR) vibrational scattering scanning near-field optical microscopy (IR *s*-SNOM) have enabled chemical nanoimaging of a wide range of systems including molecular and quantum materials [1–5]. Of particular note is nanoimaging of biological systems that exhibit structural features on mesoscopic scales ranging from proteins of nanometer dimension to membranes and cytoskeletons of multiple micrometer dimension [6–10]. These active regions that determine biological function are often sparse and separated by distances far greater than the size of the features of interest.

Desired characteristics in multispectral imaging include high spatial resolution, large field of view, and broad spectral range. However, this leads to growing datasets scaling linearly in measurement time with each spatial and spectral dimension. The associated long measurement times and compounding drift of the sample, signal, source, and detection system [11], as well as the possible diffusion in active biological systems, limit what can be achieved in conventional Fourier transform IR *s*-SNOM Fourier transform nanospectroscopy (nano-FTIR) imaging. Therefore, the application of *s*-SNOM nanospectroscopic imaging for systems with objects of interest that are sparsely distributed but spatially compact, in particular for biomaterials, has remained limited.

High-pixel-density imaging is required in multiscale composite systems as commonly encountered in many chemical or biological systems. In a mollusk shell, as a representative example, the extended shell structure is composed of $CaCO_3$ crystallites of calcite or aragonite [12]. A small amount of interspersed organic material, typically less than 5% by weight, acts as a scaffold that directs growth rates, modifies crystal habit, and controls the type of $CaCO_3$ polymorph to nucleate. However, because of its sparsity, the organic material is difficult to locate and study.

Bulk analysis of decalcified oyster shells shows that the organic component contains proteins [13–16], which are often enriched in acidic residues and which can be post-translationally modified, as well as other components like polysaccharides. Furthermore, *in situ* techniques [17–20] have localized proteins to sheath-like structures that cover individual $CaCO_3$ crystallites. However, no chemical nanoscopic characterization has yet been performed.

To address these challenges and increase imaging speed, compressive sensing has recently been applied to broadband *s*-SNOM in its implementation of synchrotron IR nanospectroscopy (SINS) [21]. In compressive *s*-SNOM, the analogous signal to be recovered is assumed to be sparse in some domain and can be fully estimated from a sub-sampled set of measurements. This offers a probabilistic approach to obtaining the desired spectral content at a drastically reduced acquisition time.

Conversely, an approach first established in nuclear magnetic resonance (NMR) involving shifting the spectroscopic carrier frequency into a "rotating frame" dramatically reduces the number

of data points required for a spectrum [22,23]. Faster acquisition through rotating frame detection is enabled through a reduction in the required number of sampled points for a given spectroscopic resolution by shifting the carrier frequency of the signal to zero. Rotating frame detection has been extended to time-domain far-field optical spectroscopy [24,25], including 2D-IR spectroscopy [26–28], enabling improved detection speed and sensitivity.

Here, we demonstrate rotating frame detection applied to IR near-field spectroscopy (R-sSNOM) and its performance in chemical imaging within the prismatic region of oyster shells. Specifically, we resolve heterogeneous nanoscale spatial protein distribution in the large scale calcite matrix in nanospectroscopic imaging based on the protein amide I IR response. In nano-FTIR with the use of an IR source of narrow bandwidth, we move into the rotating frame in order to shift the zero-point frequency to the lowest frequency of the vibrational response. Mathematically, this is analogous to a change of coordinates in the Fourier transform integral where ω is shifted by the vibrational resonant frequency ω_0 to $\omega - \omega_0$. This rotating frame s-SNOM imaging technique allows for significantly shorter spectral acquisition times and increased spatial data densities. We show a shortening in acquisition time using R-sSNOM by up to a factor of 60 compared to conventional nano-FTIR imaging. This enables higher spatial resolution imaging over large fields of view. R-sSNOM is particularly advantageous for experiments with light sources of intermediate bandwidth [2] and materials with broad vibrational resonances.

2. METHODS

A. Near-Field FTIR Spectroscopy

The IR s-SNOM experimental layout is shown in Fig. 1(a). Tunable mid-infrared (mid-IR) light is generated by difference frequency generation (DFG) by mixing signal and idler beams in a $AgGaS_2$ crystal (Harmonixx DFG, APE) from an optical parametric oscillator (Levante OPO, APE), pumped by a Yb:KGW (Flint, Light Conversion) femtosecond laser (1034 nm, pulse duration 90 fs, 6 W, 75.7 MHz repetition rate). The IR light is tunable from ~4 μm to ~15 μm (2500 to 650 cm^{-1}) with a pulse duration of 150 fs and a full width at half-maximum (FWHM) of ~100 cm^{-1}. We direct ~18 mW of DFG power, centered at 1680 cm^{-1}, into the s-SNOM instrument (nanoIR2-s prototype, Anasys Instruments). An off-axis parabolic mirror (NA = 0.45, reflected focal length = 25.4 mm) focuses the IR beam onto a gold-coated cantilever atomic force microscope (AFM) tip (160AC-GG OPUS, μmash) operating in intermittent contact (tapping) mode. The heterodyne amplified backscattered light is detected by a HgCdTe (MCT KLD-0.5-J1/DC/11, Kolmar Technologies) detector [Fig. 1(a)]. The Fourier transform of the resulting asymmetric interferogram provides the near-field spectral amplitude A($\tilde{\nu}$) and phase $\phi(\tilde{\nu})$ response of the sample at the tip location, with spatial resolution given by the tip apex radius [29]. The amplified near-field is selected by demodulating the MCT signal at the second harmonic of the tip dither frequency ω_{tip} with a lock-in amplifier (HF2LI, Zurich Instruments). Chopping the reference beam at ω_{ref} further eliminates residual far-field background and corrects for the DC baseline offset (see Supplement 1 for details). R-sSNOM nano-FTIR images are then acquired based on the near-field heterodyne signal, which is selected by lock-in demodulating at the first sideband of the near-field signal, $2\omega_{tip} + \omega_{ref}$ [10]. The spectrum is then normalized to a gold reference, which has a flat optical response across the mid-IR to good approximation. To eliminate water vapor and CO_2, we purge the IR source, AFM, reference arm, and detector enclosure with dry and CO_2-free air. The reference arm length was controlled using a linear direct-drive translation stage (Aerotech, ANT95-50-L-MP).

B. Sample Preparation

The shell of the Pacific Oyster (*Crassostrea gigas*) is a widely studied model mollusk and is characterized by a distinctive
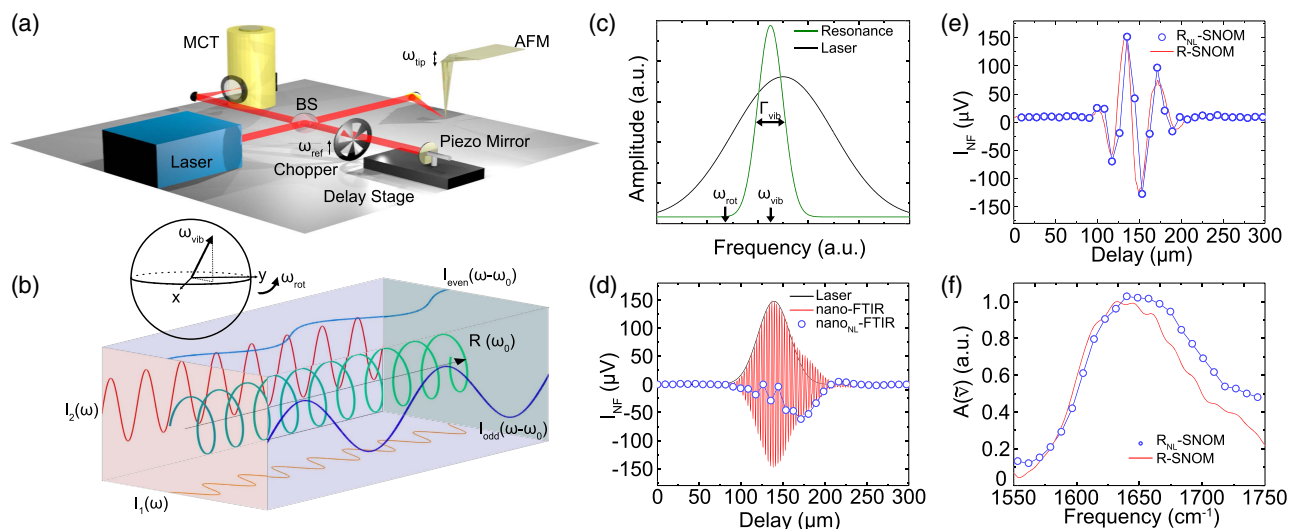

Fig. 1. Rotating Frame s-SNOM (R-sSNOM). (a) Experimental design with an IR light source and asymmetric Michelson interferometer. (b) Schematic of rotating frame reducing the frequency of the basis waveforms (red and orange) to generate new waveforms (light and dark blue) with the same information, but with the beat frequency between the rotation and basis. (c) Depiction of resonant IR feature within the IR source bandwidth. (d) Full experimental nano-FTIR interferogram (red) and a 30x subsampled interferogram that is at the Nyquist limit (blue). (e) Low-frequency full dataset nano-FTIR interferogram rotated by 1550 cm^{-1} (red) and the similarly rotated subsampled points (blue). (f) Frequency comparison of stationary (red) and rotating frame (blue) spectral response.

microstructure called the prismatic layer [30]. The prismatic layer is composed of closely packed calcite columns that are tens to hundreds of micrometers tall and are approximately 10 µm across. Each column is delimited by thin polygonal sheaths of intercrystalline organic material. Thin sections were prepared following established procedures (see Supplement 1). A quick (~3 second) and mild (0.1 M HCl) etch was performed after polishing to reexpose the organic sheath, which is preferentially removed during the polishing procedure.

C. Rotating Frame *s*-SNOM

The rotating frame is a reference frame where the Nyquist cutoff frequency is lowered, reducing the amount of data necessary for resolving a given spectral feature. The rotating frame approach is based on the rotation frequency ω_{rot}, linewidth Γ_{vib}, and center frequency ω_{vib} of the vibrational resonance to be probed [Fig. 1(c)], where ω_{rot} is less than ω_{vib} and is typically $\omega_{vib} - \Gamma_{vib}$ or smaller (see Supplement 1 for details). Figure 1(b) shows the rotating frame concept pictorially. The basis vectors (red and orange) span the rotation space and are collected as in conventional nano-FTIR with increased reference arm step size. The rotating frame analysis is then applied as a complex apodization to the collected datasets (green spiral). The recovered waveforms span the same space but have a lower apparent frequency (shown in dark and light blue). Transforming into the rotating frame is analogous to spinning a Bloch sphere, where the vibrational resonance precesses with frequency ω_{vib}, around the precession axis at the rotation frequency ω_{rot}. This results in the vibrational response being reduced by the rotation frequency $\omega_{vib} - \omega_{rot}$. We then only need to collect the near-field signal interferogram in increments of $1/\Gamma_{vib}$ over a length set by the desired spectral resolution (see Supplement 1 for details). The required step size only depends on ω_{vib}, Γ_{vib}, and ω_{rot} rather than the carrier frequency, yet is still Nyquist limited.

We first demonstrate the R-sSNOM concept through subsampling a conventionally acquired nano-FTIR dataset. Figure 1(d) (red) shows a standard nano-FTIR interferogram (stationary frame $\omega_{rot} = 0$) and a ~30 fold subsampled dataset (blue). While seemingly nonrepresentative, after transformation of both interferograms [Fig. 1(e)] into the rotating frame, the rotated and Nyquist limited (blue) and R-sSNOM (red) interferograms closely resemble each other. If we then Fourier transform the rotated interferograms and shift the frequency back by ω_{rot} to its original value, we see good agreement between the R-sSNOM (red) and the Nyquist limited R-sSNOM (blue) spectra, as shown in Fig. 1(f). Chemical imaging can now be performed approximately 60 times faster in this specific example (see Section 4 for details) while maintaining the same signal quality for each image voxel.

Following this conceptual validation of the approach, we implement R-sSNOM as a spectroscopic imaging method enabled by this dramatic reduction in sampling within the rotating frame. In this approach, we image the full sample region of interest at each reference arm delay point. The rotation process requires two basis vectors spanning the rotated space; therefore, we measure the complex-valued field at each reference arm delay using amplitude-modulated two-phase homodyne imaging as previously described [10]. We obtain spectroscopically resolved voxels by repeating the two-phase homodyne imaging at each reference arm delay, stacking the images, correcting for spatial drift, and Fourier transforming the interferogram at each pixel using the rotating frame algorithm described above. In the following example, we apply R-sSNOM spectroscopic imaging to achieve 4000 voxels at 100 nm spatial resolution, 20 cm^{-1} spectral resolution, and 200 cm^{-1} bandwidth.
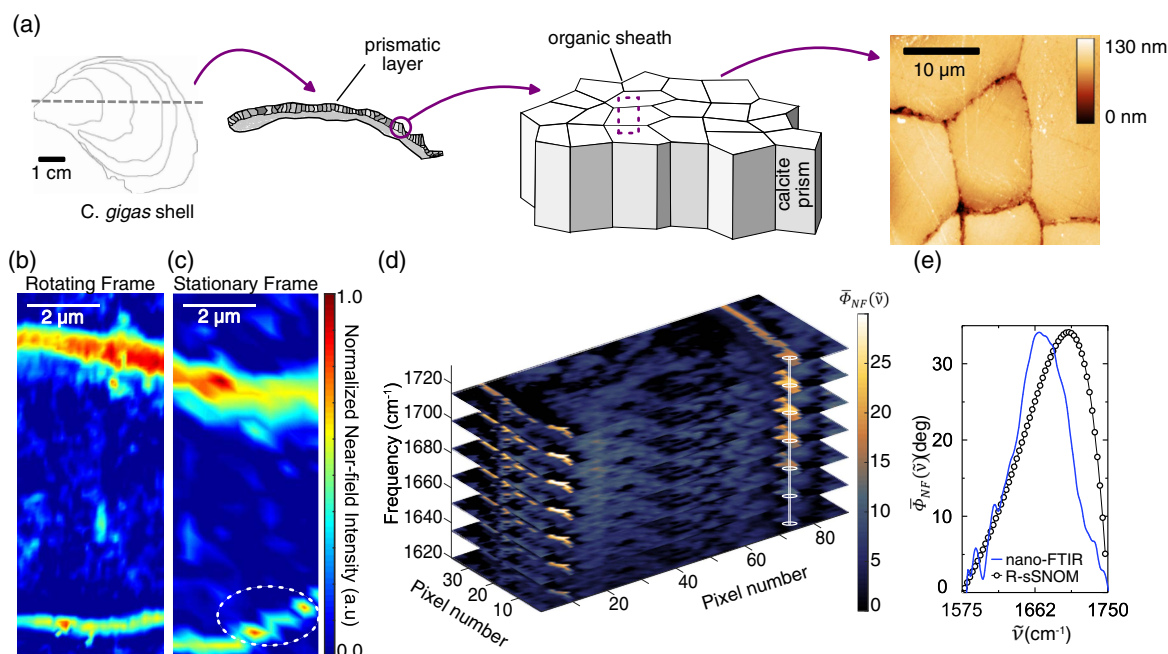

Fig. 2. Rotating frame R-sSNOM imaging. (a) The prismatic layer (middle schematic, thickness exaggerated) surrounded by organic sheaths (right). (b) Near-field scattering amplitude heterodyne amplified at zero phase difference between tip and reference arms in the rotating frame and (c) stationary frame yielding lower spatial resolution of the same region compared with (b). The white dashed line emphasizes drift artifact. (d) Spatiospectral phase image of same region acquired with R-sSNOM. (e) Representative spectrum of location indicated in (d) showing typical amide I response of the organic sheath acquired with nano-FTIR (blue) and R-sSNOM (black).

3. RESULTS

A. Protein Distribution in the Prismatic Region in an Oyster Shell

For a direct experimental comparison between conventional nano-FTIR and R-sSNOM imaging, we image the protein distribution in the prismatic region of the oyster shell. The hierarchy of scales in this biological system is shown schematically in Fig. 2(a). We center the laser at the peak of the protein specific amide I response at 1680 cm^{-1}. We chose a 4 μm by 10 μm region across a calcite crystal covering two organic sheets as indicated. For R-sSNOM, we image this region (40 by 100 pixels), with a pixel size of 100 nm by 100 nm [Fig. 2(b)]. For the conventional stationary frame nano-FTIR experiment [Fig. 2(c)], an array (10 by 30 pixels) was used, approximately 10 times fewer spatial points for the same amount of acquisition time and identical spectral resolution. An AFM image of the area was taken halfway through to characterize the AFM drift. The typical length scale (in the narrow dimension) for prismatic region features was approximately 3 voxels, or ~1 μm, wide in the conventional image. To normalize the phase spectrum, we reference to a known calcite region. This compensates for the tail end of the much stronger calcite peak, yielding a pure amide response. Figure 2(d) shows the corresponding full spatiospectral R-sSNOM phase dataset. An example spectrum from the organic region is shown in Fig. 2(e).

We now reconstruct a map of protein content by correlating AFM topography [Fig. 3(a)] with the R-sSNOM amide I phase map [Fig. 3(b)] by identifying five regions based on the calcite and amide content and their relative surface heights [Fig. 3(c)]. When compared to the topographic feature size given by the etching process, this correlation analysis identifies and locates proteins in the prismatic region with higher spatial resolution. Figure 3(d) shows the corresponding correlation diagram of height and the amide I phase response (for details, see Supplement 1). These results show that in spatiospectral imaging, where the spatial resolution needs to be relatively high, but the spectral resolution can be low, R-sSNOM provides clear benefits compared to conventional s-SNOM.

4. DISCUSSION

In the rotating frame, the scan length and step size of each interferogram are chosen such that the resulting spectral resolution and maximum measured frequency are no higher than necessary to resolve the resonances of interest. This allows for faster interferogram collection based on the reduced maximal measured frequency in the rotating frame. To effectively leverage the reduced data volume required by R-sSNOM and to increase the rate of data acquisition, we image the sample continuously, while the reference mirror is moved between images. This approach also simultaneously enables passive drift compensation (see Supplement 1 for details).

R-sSNOM has less frequent interruptions in data collection and is only paused between successive images to step the mirror position. Additionally, R-sSNOM is less sensitive to drift, as the reference mirror only needs to be stable on the ~μm scale, rather than the ~nm scale required of the AFM tip. Both of these effects result in faster and more stable multispectral chemical imaging.

In this specific experiment, we find the speed increases by a factor of ~60 for the same signal quality per voxel. As a more general example, an image with 10,000 spatial locations (100 × 100 pixel image) conventionally needs to be reimaged for conservative drift correction every 50 data points, with each image taking approximately 10 min. That reimaging time alone is longer by an order of magnitude than retrieving the complete hyperspectral image through R-sSNOM. Specifically, we demonstrate a direct comparison where, in the conventional method, to achieve 20 cm^{-1} spectral resolution, we scan the reference mirror at a rate of 10 μm/s for a total of 25 s. We sample 300 spatial positions and collect one AFM image at the beginning and one AFM image halfway through the coordinate set. Thus, the conventional imaging time is 2.3 h, generating 10 spectral data points per sample position for a total of 3000 data points of interest. This is contrasted with the R-sSNOM technique where 20 cm^{-1} resolution over 4000 sample positions yields a total of 40,000 data points in slightly less time. This corresponds to an improvement of more than an order of magnitude in acquired data points. From the accelerated acquisition, R-sSNOM not only is drift-corrected
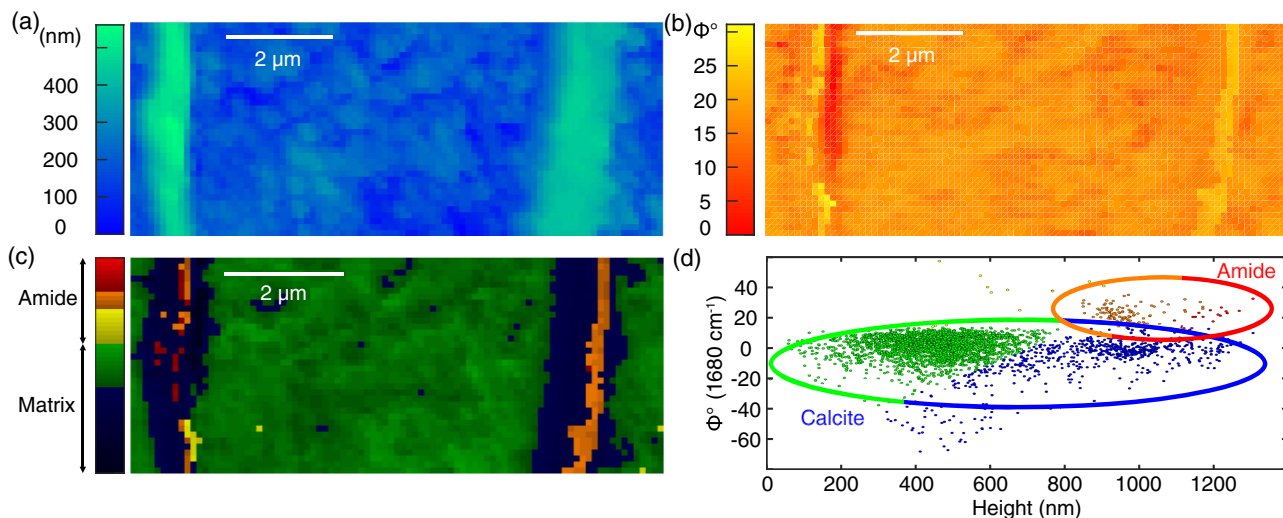

Fig. 3. Spectral and Topographic Mapping. (a) Topography from AFM. (b) Strength of near-field phase response at 1680 cm^{-1}. (c) Correlation comparison of sample topography and amide phase response. Points of high value indicate high correlation, and points of low value indicate a deviation between topography and the local amide population (see color bar). (d) Correlation plot of height and phase dependence between (a) and (b) (see color bar).

but also has a much higher spatial resolution compared to conventional nano-FTIR for the same measurement time.

When using the rotating frame approach, the first few data points of the transformation in rotation space can be slightly unstable from interference of the dual negative frequency components through frequency folding (frequencies close to the rotation frequency are not always a faithful representation). Therefore, the rotation frequency for this dataset was chosen to be 1550 cm^{-1}, i.e., away from the amide response, leading to a maximum recoverable frequency of 1750 cm^{-1} based on our choice of 200 cm^{-1} bandwidth.

In addition to the first few dropped data points near the rotation frequency, we notice the spectral accuracy in the rotating frame is not as good as that obtained using conventional methods. While simple chemical identification is still possible, the R-sSNOM measurement of the amide I response is blueshifted by ~20 cm^{-1} compared to conventional nano-FTIR [Fig. 2(e)]. Further, and in general, spectrally narrow material resonances can be measured with a lower Nyquist cutoff frequency, but they also require higher resolution to determine their peak position with sufficient accuracy. This trade-off between resolution and cutoff frequency requires measuring with larger reference arm mirror step sizes over a longer travel distance. Similarly, this trade-off exists with broader resonances with smaller step sizes over a shorter total travel distance. Materials systems with spectrally well-separated narrow resonances would therefore not benefit from R-sSNOM to the same extent, as both resolution and bandwidth need to be high.

The nanometer scale and convoluted shape of sparsely distributed organic mineral interfaces is well matched to the capabilities of R-sSNOM. The discrepancy between the length scales of the features of interest and their distribution highlights the necessity of high-resolution imaging over large spatial scales. Therefore R-sSNOM uniquely delivers chemically sensitive nanoimaging with a large field of view with an improvement of image quality, speed, and spatial resolution.

See Supplement 1 for supporting content.

REFERENCES

1. H. A. Bechtel, E. A. Muller, R. L. Olmon, M. C. Martin, and M. B. Raschke, "Ultrabroadband infrared nanospectroscopic imaging," Proc. Natl. Acad. Sci. USA **111**, 7191–7196 (2014).

2. E. A. Muller, B. Pollard, and M. B. Raschke, "Infrared chemical nanoimaging: accessing structure, coupling, and dynamics on molecular length scales," J. Phys. Chem. Lett. **6**, 1275–1284 (2015).

3. O. Khatib, H. A. Bechtel, M. C. Martin, M. B. Raschke, and G. L. Carr, "Far infrared synchrotron near-field nanoimaging and nanospectroscopy," ACS Photon. **5**, 2773–2779 (2018).

4. B. Pollard, F. C. B. Maia, M. B. Raschke, and R. O. Freitas, "Infrared vibrational nanospectroscopy by self-referenced interferometry," Nano Lett. **16**, 55–61 (2016).

5. J. Chen, M. Badioli, P. Alonso-González, S. Thongrattanasiri, F. Huth, J. Osmond, M. Spasenovi, A. Centeno, A. Pesquera, P. Godignon, A. Z. Elorza, N. Camara, F. Javier García De Abajo, R. Hillenbrand, and F. H. L. Koppens, "Optical nano-imaging of gate-tunable graphene plasmons," Nature **487**, 77–81 (2012).

6. I. Amenabar, S. Poly, W. Nuansing, E. H. Hubrich, A. A. Govyadinov, F. Huth, R. Krutokhvostov, L. Zhang, M. Knez, J. Heberle, A. M. Bittner, and R. Hillenbrand, "Structural analysis and mapping of individual protein complexes by infrared nanospectroscopy," Nat. Commun. **4**, 2890 (2013).

7. I. Amenabar, S. Poly, M. Goikoetxea, W. Nuansing, P. Lasch, and R. Hillenbrand, "Hyperspectral infrared nanoimaging of organic samples based on Fourier transform infrared nanospectroscopy," Nat. Commun. **8**, 14402 (2017).

8. A. Cricenti, R. Generosi, M. Luce, P. Perfetti, G. Margaritondo, D. Talley, J. S. Sanghera, I. D. Aggarwal, N. H. Tolk, A. Congiu-Castellano, M. A. Rizzo, and D. W. Piston, "Chemically resolved imaging of biological cells and thin films by infrared scanning near-field optical microscopy," Biophys. J. **85**, 2705–2710 (2003).

9. M. Brehm, T. Taubner, R. Hillenbrand, and F. Keilmann, "Infrared spectroscopic mapping of single nanoparticles and viruses at nanoscale resolution," Nano Lett. **6**, 1307–1310 (2006).

10. S. Berweger, D. M. Nguyen, E. A. Muller, H. A. Bechtel, T. T. Perkins, and M. B. Raschke, "Nano-chemical infrared imaging of membrane proteins in lipid bilayers," J. Am. Chem. Soc. **135**, 18292–18295 (2013).

11. M. Abe, Y. Sugimoto, T. Namikawa, K. Morita, N. Oyabu, and S. Morita, "Drift-compensated data acquisition performed at room temperature with frequency modulation atomic force microscopy," Appl. Phys. Lett. **90**, 203103 (2007).

12. F. Marin, N. Le Roy, and B. Marie, "The formation and mineralization of mollusk shell," Front. Biosci. **S4**, 1099–1125 (2012).

13. B. Marie, I. Zanella-Cléon, N. Guichard, M. Becchi, and F. Marin, "Novel proteins from the calcifying shell matrix of the pacific oyster Crassostrea gigas," Mar. Biotechnol. **13**, 1159–1168 (2011).

14. B. Marie, C. Joubert, A. Tayalé, I. Zanella-Cléon, C. Belliard, D. Piquemal, N. Cochennec-Laureau, F. Marin, Y. Gueguen, and C. Montagnani, "Different secretory repertoires control the biomineralization processes of prism and nacre deposition of the pearl oyster shell," Proc. Natl. Acad. Sci. USA **109**, 20986–20991 (2012).

15. Y. Dauphin, "Soluble organic matrices of the calcitic prismatic shell layers of two pteriomorphid bivalves," J. Biol. Chem. **278**, 15168–15177 (2003).

16. F. Marin, G. Luquet, B. Marie, and D. Medakovic, "Molluscan shell proteins: primary structure, origin, and evolution," Curr. Top. Dev. Biol. **80**, 209–276 (2007).

17. Y. Dauphin, A. D. Ball, H. Castillo-Michel, C. Chevallard, J.-P. Cuif, B. Farre, S. Pouvreau, and M. Salomé, "In situ distribution and characterization of the organic content of the oyster shell Crassostrea gigas (Mollusca, Bivalvia)," Micron **44**, 373–383 (2013).

18. Y. Dauphin, J.-P. Cuif, J. Doucet, M. Salom, J. Susini, and C. T. Willams, "In situ chemical speciation of sulfur in calcitic biominerals and the simple prism concept," J. Struct. Biol. **142**, 272–280 (2003).

19. B. Farre, A. Brunelle, O. Laprévote, J.-P. Cuif, C. T. Williams, and Y. Dauphin, "Shell layers of the black-lip pearl oyster Pinctada margaritifera: matching microstructure and composition," Comp. Biochem. Physiol. Part B **159**, 131–139 (2011).

20. F. Marin, B. Pokroy, G. Luquet, P. Layrolle, and K. De Groot, "Protein mapping of calcium carbonate biominerals by immunogold," Biomaterials **28**, 2368–2377 (2007).

21. B. Kästner, C. M. Johnson, P. Hermann, M. Kruskopf, K. Pierz, A. Hoehl, A. Hornemann, G. Ulrich, J. Fehmel, P. Patoka, E. Rü, and G. Ulm, "Infrared nanospectroscopy of phospholipid and surfactin monolayer domains," ACS Omega **3**, 4141–4147 (2018).

22. I. Rabi, N. Ramsey, and J. Schwinger, "Use of rotating coordinates in magnetic resonance problems," Rev. Mod. Phys. **26**, 167–171 (1954).
23. J. Keeler, *Understanding NMR Spectroscopy* (Wiley, 2002).
24. A. W. Albrecht, J. D. Hybl, S. M. G. Faeder, and D. M. Jonas, "Experimental distinction between phase shifts and time delays: implications for femtosecond spectroscopy and coherent control of chemical reactions," J. Chem. Phys. **111**, 10934–10956 (1999).
25. C. Scheurer and S. Mukamel, "Magnetic resonance analogies in multidimensional vibrational spectroscopy," Bull. Chem. Soc. Jpn. **75**, 989–999 (2002).
26. S.-H. Shim and M. T. Zanni, "How to turn your pump–probe instrument into a multidimensional spectrometer: 2D IR and Vis spectroscopies via pulse shaping," Phys. Chem. Chem. Phys. **11**, 748–761(2009).
27. S. K. Karthick Kumar, A. Tamimi, and M. D. Fayer, "Comparisons of 2D IR measured spectral diffusion in rotating frames using pulse shaping and in the stationary frame using the standard method," J. Chem. Phys. **137**, 184201 (2012).
28. P. L. Kramer, C. H. Giammanco, A. Tamimi, D. J. Hoffman, K. P. Sokolowsky, and M. D. Fayer, "Quasi-rotating frame: accurate line shape determination with increased efficiency in noncollinear 2D optical spectroscopy," J. Opt. Soc. Am. B **33**, 1143–1156 (2016).
29. J. M. Atkin, S. Berweger, A. C. Jones, and M. B. Raschke, "Nano-optical imaging and spectroscopy of order, phases, and domains in complex solids," Adv. Phys. **61**, 745–842 (2012).
30. G. J. Carter, "Guide to bivalve shell microstructures," in *Skeletal Growth of Aquatic Organisms* (Plenum Press, 1980), pp. 645–673.